EDGE ARTICLE

Confinement and passivation of perovskite quantum dots in porous natural palygorskite toward an efficient and ultrastable light-harvesting system in water†

Genping Meng, [‡a] Xijiao Mu,[‡a] Liping Zhen,[a] Jun Hai,[a] Zefan Zhang,[a] Tianzhi Hao,[a] Siyu Lu, [*c] Aiqin Wang [*b] and Baodui Wang [*a]

Perovskite quantum dots (QDs) are promising as representative candidates to construct next-generation superior artificial light-harvesting systems (ALHSs). However, their high sensitivity to external environments, especially to water, imposes a stringent limitation for their actual implementation. Herein, by interface engineering and encapsulation with natural palygorskite (PAL), a water-resistant light-harvesting $CsPbBr_3$@PAL antenna was prepared. Molecular dynamics simulations further confirm a significant shielding protection of the PAL matrix to $CsPbBr_3$, facilitating exceptional stability of the $CsPbBr_3$@PAL antenna when exposed to air for 10 months, to 150 °C thermal stress, and even to water for more than 30 days, respectively. Furthermore, as a result of *in situ* encapsulation of the PAL matrix and defect passivation caused by H-bonding and coordination-bonding interaction, the $CsPbBr_3$@PAL antenna in water shows a substantially enhanced photoluminescence quantum yield (36.2%) and longer lifetime. After sequentially assembling Eosin Y and Rose Bengal in the pores of the PAL matrix, RB-ESY-$CsPbBr_3$@PAL with a sequential two-step efficient Förster resonance energy transfer process exhibited extremely enhanced photocatalytic activity toward Friedel–Crafts alkylation reactions in aqueous solution, 2.5-fold higher than that of corresponding ESY/RB. Our work provides a feasible strategy for the exploitation of ultra-stable halide perovskite-based ALHSs in aqueous media for solar-energy conversion.

1. Introduction

In nature, photosynthesis is the basic element for plants and other organisms to obtain life-sustaining energy, while helping to keep the terrestrial environment suitable for the survival of other living things.[1–3] Inspired by nature, many scientists have begun to pay attention to the development of artificial light-harvesting systems (ALHSs),[4–7] which have promoted the remarkable development in optoelectronic and photonic materials and devices such as photocatalysis,[7–10] solar cells,[11–14] optical sensors,[15–18] and luminescent materials.[19–22] However, most of the reported sophisticated ALHSs are manufactured in organic solvents rather

than in aqueous media as in nature, which hinders their actual applications. Due to the limitations of the solubility of hydrophobic chromophores in water and the quenching effect caused by undesirable aggregation, ALHSs constructed in an aqueous environment usually show unsatisfactory performance.[8,23] In addition, only a few studies focused on the natural sequential Förster resonance energy transfer (FRET) process,[8] which could achieve larger Stokes shifts and more efficient FRET even without any spectral overlap and/or beyond the Förster radius. Therefore, it is still a challenge to design and fabricate highly efficient ALHSs with the sequential FRET process in an aqueous environment.

Perovskite quantum dots (QDs) have attracted tremendous attention as promising candidates for photovoltaic and optoelectronic device applications,[24–27] and they possess outstanding optoelectronic properties, such as a high quantum yield (QY), tunable electronic bandgaps and emission spectra in the visible range, narrow emission line widths, and a high molar extinction coefficient.[28–30] These advantages make perovskite QDs an attractive alternative to highly efficient light-harvesting antennas for collecting solar energy in ALHSs.[31–34] Despite enormous efforts, due to phase transition in water vapor or the aggravation of lattice vibration at high temperature,[35,36] the reported perovskite-based ALHSs were only employed in organic solvents

aState Key Laboratory of Applied Organic Chemistry, Key Laboratory of Nonferrous Metal Chemistry and Resources Utilization of Gansu Province, Lanzhou University, Gansu, Lanzhou 730000, China. E-mail: wangbd@lzu.edu.cn

bKey Laboratory of Clay Mineral Applied Research of Gansu Province, Lanzhou Institute of Chemical Physics, Chinese Academy of Sciences, Lanzhou, Gansu 730000, China. E-mail: aqwang@licp.cas.cn

cCollege of Chemistry and Molecular Engineering, Zhengzhou University, Zhengzhou 450001, China. E-mail: sylu2013@zzu.edu.cn

† Electronic supplementary information (ESI) available. See https://doi.org/10.1039/d2sc05220b

‡ These authors contributed equally to this work.

and under mild conditions. Therefore, it is a daunting task to realize perovskite-based ALHSs with the sequential FRET regime in aqueous environments, and it has not yet been basically fulfilled. To overcome these obstacles, numerous porous materials such as crosslinked polystyrene beads, zeolites, amorphous alumina and metal–organic frameworks have demonstrated promise for shielding protection of perovskite QDs,[37–40] which significantly improved the water and thermal stabilities of perovskite QDs. However, so far, these strategies have not been used to construct ultrastable and efficient perovskite-based ALHSs with the sequential FRET process in aqueous environments.

Palygorskite (PAL)[41–44] is a category of natural earth-abundant magnesium aluminum silicate crystalline minerals possessing moderate cation-exchange capacity and regular 3D zeolite-like channels. In such circumstances, porous PAL has provided better confinement and encapsulation for potentially luminescent dye molecules and perovskite QDs owing to their more tunable pores and specific sites though post-processing.[5,45–47] Typically, magnesium aluminosilicate layers contain exchangeable cations such as Mg^{2+}, K^+ and Na^+. These native species can be ion-exchanged for other metal ions,[48–51] so that lead ions can be encapsulated through the ion-exchange process. The surface of the PAL channel contains plentiful functional groups, including Si–OH, Mg–OH, and Al–OH, all of which can form H-bonds and coordination bonds with the halide anions and lead ions of the perovskite QDs, respectively. Moreover, PAL could serve as a host matrix to guide the restricted growth of $CsPbBr_3$ QDs and isolate them from each other to diminish the aggregation-caused quenching (ACQ) effect, which enables significantly improved stability and luminescence performance of the perovskite. Motivated by the above inspirations, we demonstrated in situ growth of $CsPbBr_3$ QDs in a porous PAL matrix to construct an efficient water-resistant light-harvesting antenna (denote as

$CsPbBr_3$@PAL). The resulting $CsPbBr_3$@PAL composite exhibits ultrastable emission in water for more than 30 days, and it can be further used to encapsulate fluorescence dye Eosin Y (ESY) and Rose Bengal (RB) (Fig. S1†) to build an efficient and ultrastable ALHS (RB-ESY-$CsPbBr_3$@PAL), which could implement an efficient sequential two-step energy-transfer regime in aqueous solution (Fig. 1). Significantly, the harvested solar energy of the RB-ESY-$CsPbBr_3$@PAL system could efficiently promote the photocatalyzed Friedel–Crafts alkylation reactions in aqueous medium due to the in situ encapsulation- and defect passivation-enhanced Förster resonance energy transfer (FRET) process. To the best of our knowledge, it is the first time to fabricate an efficient and water-resistant light-harvesting system using perovskite QDs enabled by chemical interface engineering and encapsulation with natural palygorskite. Therefore, our work is an interesting concept that advances the use of perovskites as a light-harvesting antenna in water.

2. Results and discussion

2.1 Preparation and characterization of the perovskite–palygorskite antenna

As a proof-of-concept experiment, we rationally designed $CsPbX_3$@PAL (X = Cl, Br or I) composite light-harvesting antennas. In a typical procedure, Fig. 1 shows a schematic illustration of the preparation of the perovskite–palygorskite composite antenna and its sequential two-step energy transfer system (vide infra). The PAL matrix was first treated with hydrochloric acid according to literature protocols to form considerable numbers of silanol groups (Si–OH) and eliminate carbonate impurities of intracrystalline tunnels (Fig. S2†).[52–54] The transmission electron microscopy (TEM) images (Fig. S3†) and powder X-ray diffraction (PXRD) patterns (Fig. S4†) showed
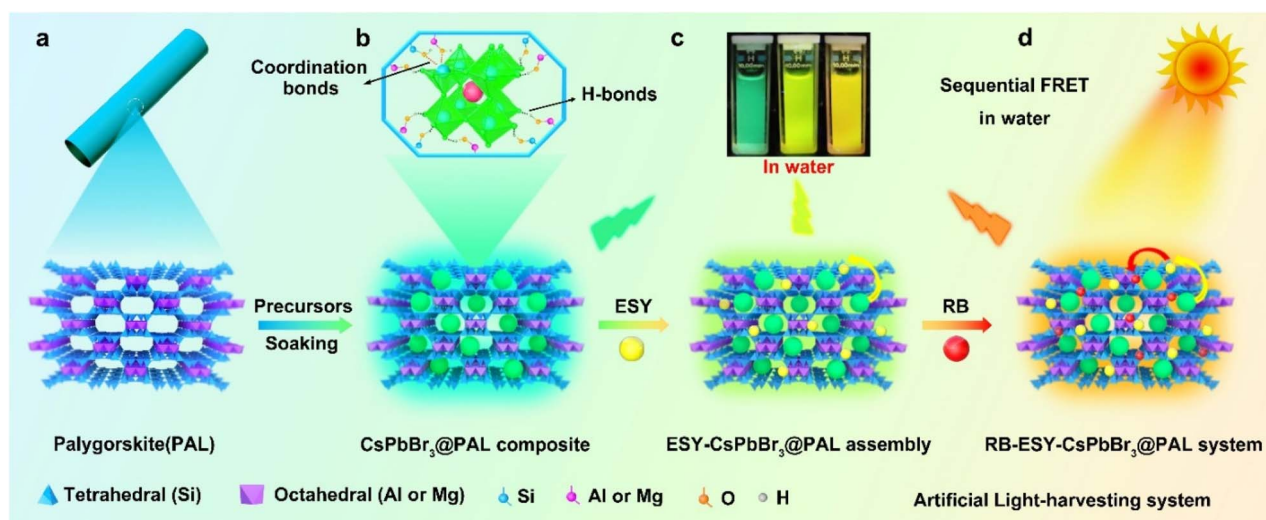

Fig. 1 Schematics of the construction of the perovskite–palygorskite composite-based ALHS and the light-harvesting process. (a) The projection of the PAL structure along the (001) direction illustrates its porous nature. (b) Preparation of the water-resistant light-harvesting $CsPbBr_3$@PAL antenna. Illustration of the $CsPbBr_3$ QDs confined in the PAL matrix, showing H-bonding and coordination-bonding interactions between the PAL matrix and perovskite QDs. The Cs^+ ion is shown as one red sphere and the $PbBr_6^{4-}$ octahedra are shown in green. (c) and (d) Construction of the ALHS with sequential two-step energy transfer in water.

that the PAL maintained the fibrous morphology and strong (110) crystal plane during the treating process. However, its pore size has been expanded to 3–6 nm (Fig. S5†). Then, the as-treated PAL was immersed in precursor solution of $PbBr_2$ at 80 °C for a week.[55,56] Elemental composition analyses (Fig. S6 and Table S1†) showed that the content of Mg^{2+}, Na^+ and K^+ decreased and the content of Pb^{2+} and Br^- increased after ion exchange, which further confirmed that the ion exchange process occurs. Subsequently, the free $PbBr_2$ was washed with DMF/ethanol by centrifugation. The obtained $PbBr_2$@PAL was dispersed in DMF solution containing Cs-Oleate and subjected to an ultrasonic reaction. Finally, the reaction mixture was precipitated in toluene at room temperature[57] to obtain a PAL-encapsulated perovskite composite (denoted as $CsPbBr_3$@PAL composite), where $CsPbBr_3$ QDs *in situ* nucleated and crystallized inside the PAL matrix (for a full description of the methods, see the ESI†). Such a PAL protection strategy could diminish the ACQ effect and environmental sensitivity, because of the *in situ* encapsulation and the defect passivation of the PAL matrix.

The framework and topological structure of the PAL matrix could guide the restricted growth of $CsPbBr_3$ QDs and keep them isolated from each other, where strong H-bonding and coordination bonding were formed between the hydroxyl group of the PAL matrix and the halide anions and lead ions of the $CsPbBr_3$ QDs, respectively. Such *in situ* encapsulation and defect passivation enable the improvement of luminescence performance and stability, suggesting that the $CsPbBr_3$@PAL composite could be an attractive alternative to serve as a light-harvesting antenna. Firstly, the structure of the $CsPbBr_3$@PAL antenna was synthetically confirmed. The SEM image (Fig. S7a†) shows that the $CsPbBr_3$@PAL antenna has a fibrous morphology. No free $CsPbBr_3$ QDs were observed, indicating that $CsPbBr_3$ QDs were mainly encapsulated in the PAL matrix. Transmission electron microscopy (TEM) studies revealed that $CsPbBr_3$ QDs were dispersed in the pores of the PAL matrix with an average diameter of 4.4 nm (Fig. 2a and S7b†), and the size of $CsPbBr_3$ QDs matches well with the mesoporous pores of the PAL matrix (Fig. S8†), preliminarily suggesting that the growth of perovskite QDs can be well encapsulated by the cavities of the natural PAL matrix. This phenomenon has also been observed in a previous perovskite-zeolite composite.[39] Fig. 2b clearly shows the isolated $CsPbBr_3$ QDs with high crystallinity in the $CsPbBr_3$@PAL composite. The representative high-resolution TEM (HRTEM) image shows a well-defined lattice spacing from fringes of about 2.92 Å (inset in Fig. 2b), which matches well with the (200) crystal faces of the cubic phase structure of $CsPbBr_3$ with the *Pm3m* space group, further suggesting that $CsPbBr_3$ QDs were formed in the mesoporous cages of the PAL matrix. The electron diffraction pattern (Fig. 2c) confirms the high crystallinity of $CsPbBr_3$ QDs in the $CsPbBr_3$@PAL composite.[58] To better characterize the structure of $CsPbBr_3$ QDs, a HRTEM was used to obtain the atomic image. As presented in Fig. 2d, the HRTEM image can individually resolve the atomic regular distribution of Pb from the <111> projection. To further verify the successful preparation of the composite material, the scanning transmission electron microscopy high-
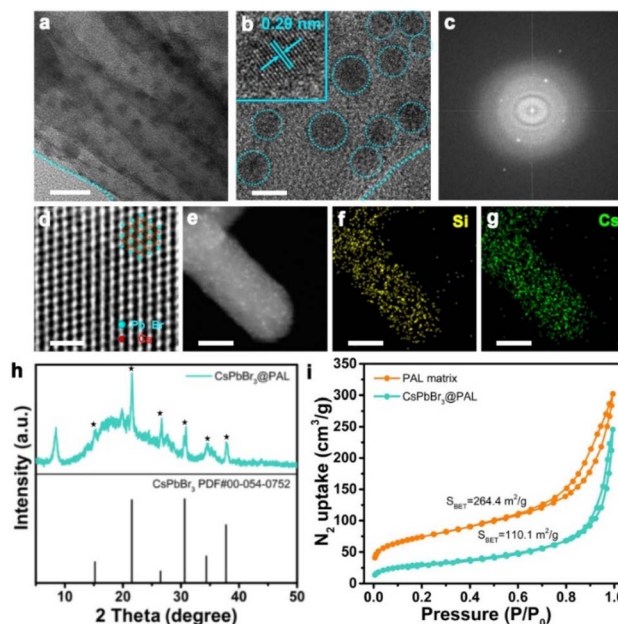

Fig. 2 Characterization of the $CsPbBr_3$@PAL antenna. (a) and (b) TEM image of the $CsPbBr_3$@PAL antenna; the black dots are $CsPbBr_3$ QDs. Inset shows the HRTEM image of (b) the lattice spacing of the confined $CsPbBr_3$ QDs. (c) The electron diffraction pattern of $CsPbBr_3$ QDs in the $CsPbBr_3$@PAL composite. The electron diffraction pattern reveals the high crystallinity of the $CsPbBr_3$ QDs. (d) Magnified HRTEM image of $CsPbBr_3$ QDs showing an atomic arrangement from the <111> projection. (e) HAADF image of PAL filled with $CsPbBr_3$ QDs. (f) and (g) The Si and Cs elemental mapping by EDX on the same area. Scale bars: (a) 20 nm; (b) 5 nm; (d) 1 nm; (e), (f), and (g) 30 nm. (h) PXRD patterns of the $CsPbBr_3$@PAL composite. (i) N_2 sorption isotherm at 77 K and Brunauer–Emmett–Teller plot (inset) for the $CsPbBr_3$@PAL composite.

angle annular dark-field (STEM-HAADF) image of the $CsPbBr_3$@PAL antenna clearly shows the $CsPbBr_3$ QDs in the PAL matrix (Fig. 2e), and the corresponding area-selective energy-dispersive X-ray spectroscopy (EDX) mappings (Fig. 2f, g and S9†) further reveal the presence and dispersion of the $CsPbBr_3$ QDs in the PAL matrix. Furthermore, we carried out PXRD measurements for evaluating the crystallinity of the $CsPbBr_3$@PAL antenna (Fig. 2h). The experimental results show characteristic structural peaks at 21.55, 26.48, 30.65 and 37.77°, which are well indexed to the (110), (111), (200) and (211) planes of the $CsPbBr_3$ bulky sample (*Pm3m*, space group No. 221, PDF No. 00-054-0752), respectively. But the peaks of $CsPbBr_3$ QDs are weaker, indicating the formation of $CsPbBr_3$ QDs within the PAL matrix. Brunauer–Emmet–Teller (BET) studies (Fig. 2i, S8 and Table S2†) further support the encapsulation of $CsPbBr_3$ QDs in the PAL matrix. The pore volumes and specific surface area are calculated to be 0.38 $m^3\,g^{-1}$ and 110.1 $m^2\,g^{-1}$ for the $CsPbBr_3$@PAL antenna, respectively, and 0.47 $m^3\,g^{-1}$ and 264.4 $m^2\,g^{-1}$ for the PAL matrix, respectively. The pore volume and N_2 uptake capacity at saturation are decreased by 19.1% and 58.4% after the encapsulation of $CsPbBr_3$ QDs, respectively, demonstrating the *in situ* growth of $CsPbBr_3$ QDs into the internal pores of the PAL matrix.[39,58] The above results prove that the $CsPbBr_3$@PAL antenna has been successfully built through

a simple and rational design. The $CsPbBr_3$ QDs are encapsulated in the pores of the PAL matrix through absorption and cation-exchange processes, in which strong H bonds and coordination bonds can be formed between the plentiful dangling functional groups of the PAL matrix including Si–OH, Al–OH, and Mg–OH and the halide anions and lead ions of $CsPbBr_3$ QDs, respectively. From the Fourier Transform Infrared (FTIR) spectra in Fig. S10,† compared to the PAL matrix, the

$CsPbBr_3$@PAL antenna exhibits a wider –OH vibrational peak with a slight shift to a lower wavenumber, which reveals the presence of H bonds between the bromide anion of the $CsPbBr_3$ QDs and the hydroxyl groups on the PAL matrix. Zhao et al. also reported this H-bonding interaction previously between $MAPbBr_3$ QDs and the Al–OH, P–OH, and P=O groups of AlPO-5 zeolite.[39,59] The X-ray photoelectron spectra (XPS) exhibit the characteristic peaks of Cs, Pb, Br, C, Si, Al and O, which are
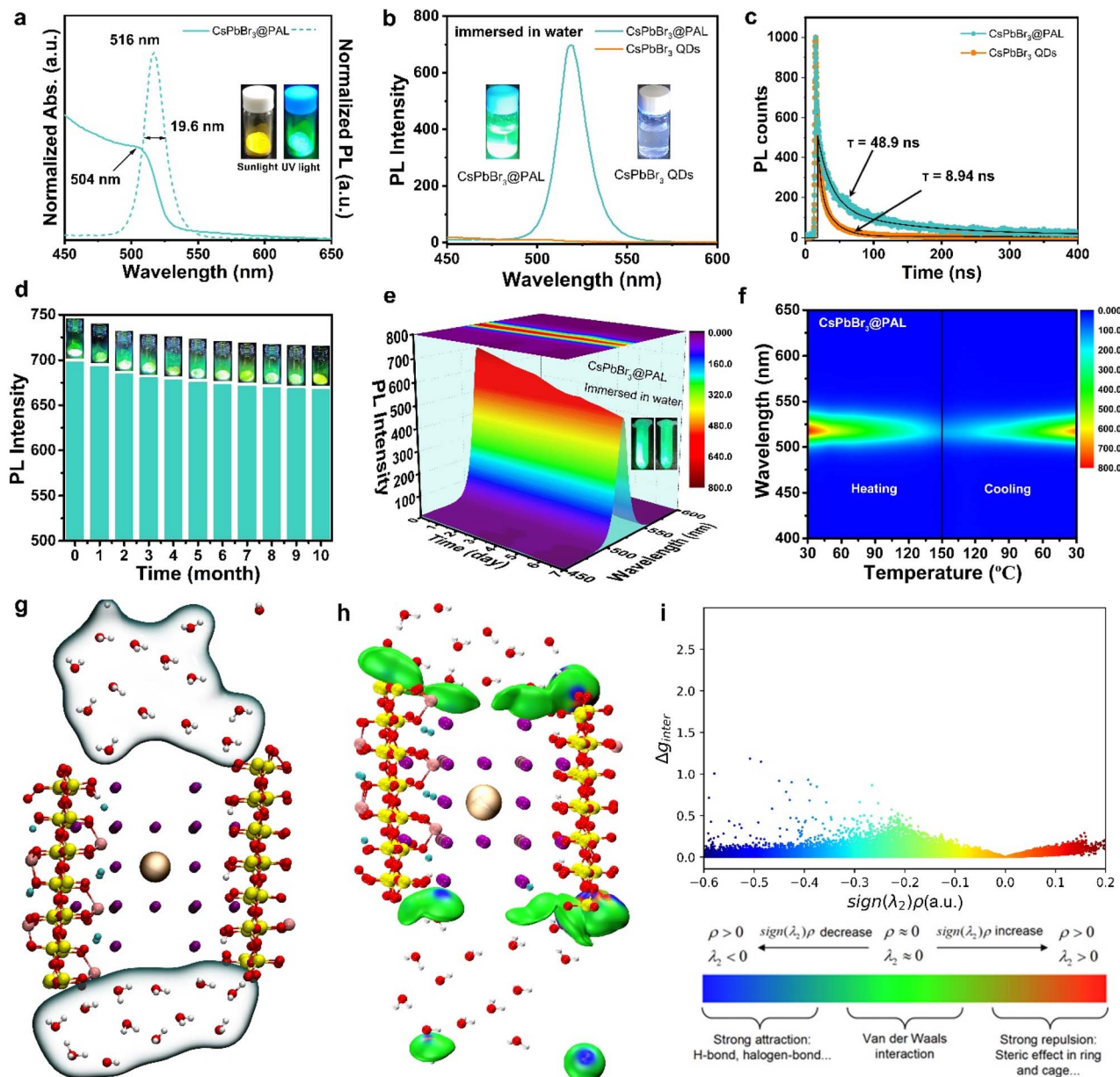

Fig. 3 The optical properties and stability of the $CsPbBr_3$@PAL antenna. (a) UV/Vis DRS (solid lines) and PL (dotted lines) spectra of the $CsPbBr_3$@PAL antenna. Inset: digital photograph of the $CsPbBr_3$@PAL antenna taken under a 365 nm xenon lamp. (b) The PL spectra of the $CsPbBr_3$@PAL antenna and neat $CsPbBr_3$ QDs in water. (c) TRFDS spectra of the $CsPbBr_3$@PAL antenna. The black curves are the fitting curves of the two PL decay curves, respectively. (d) PL intensity of the stored $CsPbBr_3$@PAL antenna stored in air environments for 10 months. Inset: corresponding digital photos under ultraviolet irradiation at 365 nm. (e) 3D Colour Map Surface image of the PL spectrum of the $CsPbBr_3$@PAL antenna immersed in water for a week. Inset: digital photos under ultraviolet irradiation at 365 nm before and after immersion in water. (f) Pseudo-colour image of the temperature-dependent PL for the $CsPbBr_3$@PAL antenna, including heating up and cooling down processes. (g) Molecular dynamics equilibrium structure of the composite $CsPbBr_3$@PAL and water. (h) Equivalent surface diagram of the independent gradient model. (i) Scatter plot.

consistent with the elements in the CsPbBr$_3$@PAL antenna (Fig. S11a†). The binding energy related to the oxygen signal shifts from 527.0 eV for the PAL matrix to 527.5 eV for the CsPbBr$_3$@PAL antenna (Fig. S11b and c†). This phenomenon implies that the formation of O–Pb coordination bonds leads to a decrease in the electron density of O atoms.[60] Therefore, the cation-exchange properties of the PAL matrix could realize the confined growth of perovskite QDs, which enables the *in situ* encapsulation of CsPbBr$_3$ QDs. Strong H-bonding and coordination-bonding interactions not only improve the cohesion of CsPbBr$_3$ QDs with the PAL matrix, but also passivate the surface defects of CsPbBr$_3$ QDs, which enhances the luminescence performance and stability of perovskite.

The obtained CsPbBr$_3$@PAL antenna shows a yellow powder, indicating the formation of the CsPbBr$_3$@PAL composite.[61] The as-synthesized CsPbBr$_3$@PAL antenna exhibits strong green fluorescence emission under UV irradiation with a wavelength of 365 nm (Fig. S12†). To verify that the strong photoluminescence of the CsPbBr$_3$@PAL antenna is derived from encapsulation and defect passivation, neat CsPbBr$_3$ QDs with an average size of 4.3 nm were synthesized (Fig. S13†). Fig. S12† shows that the CsPbBr$_3$ QDs emit faintly negligible fluorescence under ultraviolet irradiation, caused by the typical non-radiative recombination at the defects of CsPbBr$_3$ QDs.[39] Benefiting from the encapsulation and *in situ* passivation in the PAL matrix, the antenna exhibits good optical properties. UV/Vis diffuse reflectance spectroscopy (DRS) of CsPbBr$_3$@PAL shows a well-resolved band-edge exciton peak at a wavelength of *ca.* 504 nm (Fig. 3a) and the direct band gap is calculated from Tauc plots to be approximately 2.37 eV (Fig. S14†), which is analogous to previously reported perovskite composites.[39,62] Impressively, the photoluminescence (PL) of CsPbBr$_3$ QDs embedded into the PAL matrix exhibits a sharp emission peak at 516 nm (Fig. 3a), blue-shifted by ≈ 21 nm with respect to the CsPbBr$_3$ bulk crystals (BCs) (Fig. S15†). This could be connected with the quantum-confinement effect.[63–65] Moreover, for the CsPbBr$_3$@PAL antenna, the emission line width of the PL peak is 19.6 nm. Such a narrow PL peak width of the composite material is due to the encapsulation of CsPbBr$_3$ QDs by the PAL matrix, which cause the reduction of the size distribution range of CsPbBr$_3$ QDs.[66,67] More importantly, Fig. 3b shows that the neat CsPbBr$_3$ QDs decomposed easily in water and show negligible fluorescence. However, the CsPbBr$_3$@PAL composite still retains strong fluorescence emission in water. To further confirm defect passivation caused by H-bonding and coordination-bonding interactions, time-resolved fluorescent decay spectroscopy (TRFDS) of traces was performed and the results are shown in Fig. 3c and Table S3.† Two curves, a faster one for the CsPbBr$_3$ QDs and a slower one for the CsPbBr$_3$@PAL antenna, were obtained and the slower decay means a longer lifetime. Meanwhile, the decay curves were fitted, respectively, with a fast decay relevant to the high defect sites on the crystal surface and a slow decay relative to the carrier transport inside the quasi-perfect crystals.[39] The short and long lifetimes of the CsPbBr$_3$@PAL antenna are computed to be $\tau_1 = 19.61$ ns and $\tau_2 = 121.64$ ns, respectively, almost 5-fold and 6-fold that of the CsPbBr$_3$ QDs (Table S3†). This alludes that the CsPbBr$_3$ QDs within the PAL matrix have a much lower defect density. The nonradiative recombination and the shortened lifetimes observed in the CsPbBr$_3$ QDs might originate from the formation of anti-site Pb–Br defects and vacancies, which is due to under-coordinated Pb atoms.[39,68,69] Therefore, H-bonding and coordination-bonding interactions between the functional hydroxyl groups of the PAL matrix and the CsPbBr$_3$ QDs play a key role in passivating the surface defects and suppressing ion migrations. The as-obtained CsPbBr$_3$@PAL antenna displays enhanced PL emission, which benefits from the *in situ* encapsulation and defect passivation of the PAL matrix. Therefore, the absolute QY of the CsPbBr$_3$@PAL antenna reaches 36.2% (Fig. S16†) in water, which is higher than that of CsPbBr$_3$–zeolite-Y, CsPbBr$_3$–SiO$_2$ and CsPbBr$_3$–AlPO-5 composite phosphors.[37,39,64] However, the CsPbBr$_3$ QDs have almost no PL (Fig. S17†) in water, which is in agreement with previous reports about the low QY for perovskite QDs without ligand passivation or matrix encapsulation.[29,39]

2.2 Evaluation of ambient, water and thermal stability of the CsPbBr$_3$@PAL antenna

To probe the stability toward air, the CsPbBr$_3$@PAL antenna was exposed to ambient conditions with $\approx 40\%$ humidity for 10 months. The specimen still exhibits remarkable PL performance (Fig. 3d), and the PL intensity of the CsPbBr$_3$@PAL antenna dropped by only 4.4%. Such excellent ambient stability demonstrates that the PAL matrix can effectively diminish the contact of the CsPbBr$_3$ QDs with the external moisture on account of the shielding protection and passivation of the PAL matrix.[37,70] Paramount to this feature, the CsPbBr$_3$@PAL antenna exhibits striking water durability. To obtain more direct evidence, the specimen was ultrasonically soaked in water to monitor PL intensity. It can still show 74.1% luminescence under ultraviolet irradiation after a week, as presented in Fig. 3e and S18a.† After 30 days, the sample in water still maintains a certain fluorescence emission (Fig. S18b†). The prominent ambient and water stabilities of the antenna suggest that the PAL matrix can effectively protect CsPbBr$_3$ QDs and suppress the decomposition of CsPbBr$_3$ QDs by water. Additionally, the thermal stability was investigated by monitoring the PL intensity of the CsPbBr$_3$@PAL antenna during a heating–cooling cycle at 30–150 °C. As presented in Fig. 3f and S19.† The PL emission intensity of the CsPbBr$_3$@PAL antenna reduces with the increase of the temperature in the heating phase, which may be ascribed to more non-radiative transitions that stem from the intensified lattice vibration.[39] The PL intensity of CsPbBr$_3$@PAL can maintain 47.7% and 17.3% of its initial PL value at 90 °C and 150 °C, respectively. Intriguingly, the PL intensity of CsPbBr$_3$@PAL could progressively recover to 89.5% of its initial PL value after cooling down to 30 °C. These results demonstrate that the PAL matrix can productively suppress the lattice vibration of the perovskite QDs at high temperature.

To further understand the stability of CsPbBr$_3$ in water, we employed molecular dynamics simulations to investigate the interaction between water and CsPbBr$_3$@PAL. Fig. 3g shows that water molecules cannot enter the cavity of PAL, thus reducing the quenching of perovskite by water. Further
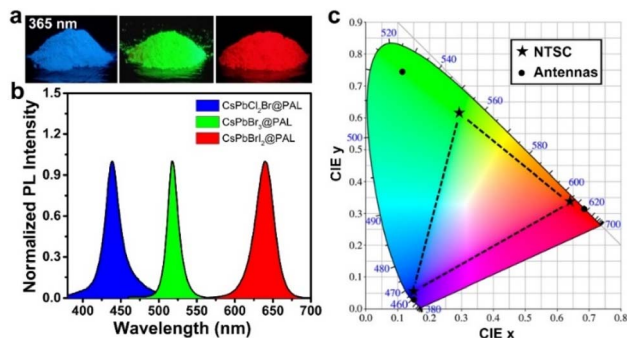
Fig. 4 Composition-tunable PL spectra of the CsPbX$_3$@PAL composite. (a) Digital photos of the CsPbX$_3$@PAL composite under ultraviolet irradiation at 365 nm. (b) PL spectra of the CsPbX$_3$@PAL composite. (c) CIE coordinates of the three-color CsPbX$_3$@PAL composite (circular) compared to the NTSC color standards (stars).

interaction analysis showed the existence of van der Waals forces between water and the cavity (Fig. 3h). The scatter plot also shows that the existence of surface tension of water molecules makes it difficult for water molecules to enter the cavity of PAL (Fig. 3i). These results indicate that the PAL in CsPbBr$_3$@PAL can efficiently prevent the contact between water and CsPbBr$_3$ QDs, thereby greatly improving the water stability of perovskite. Notably, CsPbX$_3$@PAL (X = Cl, Br or I) composites can accurately achieve color tunable emission under the excitation of UV light (Fig. 4a). Fig. 4b clearly shows that the normalized PL spectra can be effectively tuned in the range from 438 to 640 nm by introducing the Cl and I halogen anions, which is conducive to achieving overlap as considerable as possible between the CsPbX$_3$@PAL antenna emission and the dye molecule absorption. Fig. S20† shows more detailed spectral information. All specimens exhibit extremely pure and saturated colors, as presented in the Commission Internationale de l'Eclairage (CIE) chromaticity diagram (Fig. 4c). Compared to the National Television System Committee (NTSC) standard colors (stars), the color-tunable CsPbX$_3$@PAL antennas can cover the upper left part of the CIE diagram. Therefore, the CsPbX$_3$@PAL composites can be used as an extraordinary antenna candidate to construct ALHSs.

2.3 Construction of an artificial light-harvesting system with sequential two-step energy transfer in water

Taking the above considerations into account, it is feasible to construct an efficient ALHS with a sequential two-step FRET regime, in which the effective transfer of solar energy from the CsPbBr$_3$@PAL donor to the dye acceptors can be implemented. ESY dye was selected as the first acceptor, because the fluorescence spectrum of the CsPbBr$_3$@PAL antenna overlapped well with the absorption spectrum of ESY dye (Fig. S21a†). As depicted in Fig. 5a, with the progressive increase of the ratio of the ESY acceptor to the CsPbBr$_3$@PAL antenna, the PL intensity of the ESY acceptor at 541 nm gradually appeared and increased as indicated by emission spectra, while the PL intensity of the CsPbBr$_3$@PAL antenna at 516 nm decreased upon excitation under 365 nm illumination in water. In contrast, the PL

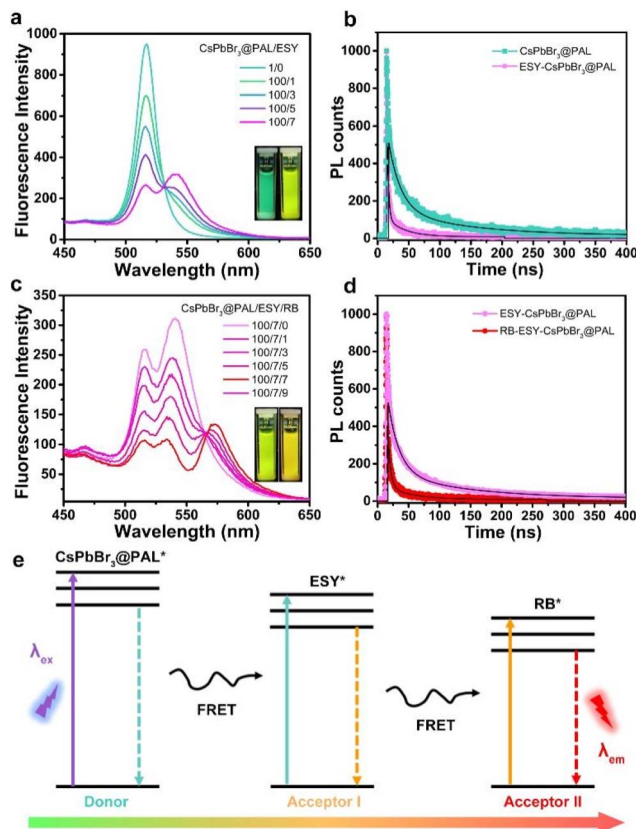**Fig. 5** Artificial light-harvesting system with sequential energy transfer. Emission spectra of the CsPbBr$_3$@PAL antenna with different amounts of ESY receptor (a) and ESY-CsPbBr$_3$@PAL (100 : 7) with different amounts of RB receptor (c) in water (λ_{ex} = 365 nm). The illustrations are digital photos. The TRFDS spectra of the CsPbBr$_3$@PAL antenna and ESY-CsPbBr$_3$@PAL recorded at λ = 516 nm (b) and ESY-CsPbBr$_3$@PAL and RB-ESY-CsPbBr$_3$@PAL recorded at λ = 541 nm (d) in water (λ_{ex} = 365 nm). (e) Illustration of the energy level diagram for sequential FRET-associated PL.

intensity of free ESY was negligible upon direct excitation at 365 nm (Fig. S22a†). Moreover, the visual fluorescent color changed from green of the CsPbBr$_3$@PAL antenna to yellow-green of the ESY-CsPbBr$_3$@PAL assembly, obviously implying efficient energy transfer from the CsPbBr$_3$@PAL antenna to the ESY acceptor. In addition, the TRFDS tests showed that the fluorescence lifetimes (τ) declined from the CsPbBr$_3$@PAL antenna (τ_1 = 19.61 ns and τ_2 = 121.64 ns) to the ESY-CsPbBr$_3$@PAL assembly (τ_1 = 2.21 ns and τ_2 = 29.00 ns) (Fig. 5b and Table S5†), demonstrating that the collected photons by the CsPbBr$_3$@PAL antenna were successfully transported to the ESY acceptor. Moreover, based on the TRFDS of ESY (Fig. S23 in the ESI†), the average lifetime (τ) of EYB (λ_{ex} = 516 nm) was 2.9 ns, providing more evidence for the energy transfer from the CsPbBr$_3$@PAL donor to the ESY acceptor. In the ESY-CsPbBr$_3$@PAL assembly, the energy transfer efficiency (Φ_{ET}) eventually reached 72.2% at a donor/acceptor ratio of 100 : 7 in water (Fig. S24a, b and Table S6†).
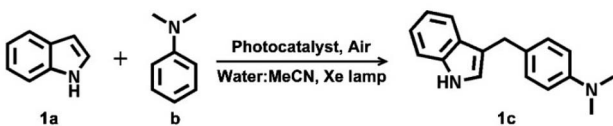
Considering that the natural light-harvesting process features sequential multistep FRET, we further constructed a sequential

two-step FRET system by using the CsPbBr$_3$@PAL antenna. RB was selected as the second acceptor, because its absorption spectrum and the fluorescence spectrum of the ESY-CsPbBr$_3$@PAL assembly matched well (Fig. S21b†). With the gradual increase of the ratio of the RB acceptor to the ESY-CsPbBr$_3$@PAL assembly, the PL intensity at 570 nm ascribed to RB burgeoned and progressively increased, while the emission peak of ESY at 541 nm decreased upon excitation under 365 nm illumination in water (Fig. 5c), along with visual changes from yellow-green to orange in the fluorescence color. In contrast, the PL intensity of free RB was negligible upon direct excitation at 365 nm (Fig. S22b†). In the RB-ESY-CsPbBr$_3$@PAL system, the second-step energy transfer efficiency was calculated to be 65.3% (Fig. S24c, d and Table S6†) at a CsPbBr$_3$@PAL : ESY : RB ratio of 100 : 7 : 9. A decline of the fluorescence lifetime (τ), from the ESY-CsPbBr$_3$@PAL assembly ($\tau_1 = 18.04$ ns and $\tau_2 = 121.89$ ns) to the RB-ESY-CsPbBr$_3$@PAL system ($\tau_1 = 4.31$ ns and $\tau_2 = 41.94$ ns) (Fig. 5d and Table S5†), was recorded by TRFDS experiments. Moreover, the TRFDS of RB (ESI,† Fig. S23†) shows that the average lifetime (τ) of RB ($\lambda_{ex} = 541$ nm) was 1.0 ns, providing more evidence for the sequential two-step energy transfer. These results suggest that the CsPbBr$_3$@PAL composite successfully behaves as a donor in ALHS, and sequential two-step FRET instead of charge transfer[34] is achieved from the CsPbBr$_3$ QDs to ESY, and then to RB in the relay mode (Fig. 5e). More importantly, as presented in Fig. S25,† the CsPbBr$_3$@PAL antenna remains dispersed for at least 24 h at room temperature, indicating that the hydrophily of the PAL matrix can restrain its agglomeration and improve its dispersity in water.

Furthermore, in order to illustrate that it is the combination of the PAL matrix and perovskite QDs that endows the CsPbBr$_3$@PAL antenna with excellent performance, the CsPbBr$_3$ QDs with an average size of 4.3 nm are used as an antenna to construct an ALHS for comparison. Fig. S17† shows that the CsPbBr$_3$ QDs without the PAL matrix decomposed easily in water and show negligible fluorescence. Therefore, CsPbBr$_3$ QDs without the PAL matrix fail to construct an ALHS in water. When CsPbBr$_3$ QDs and ESY were dispersed in toluene, an inconspicuous FRET process was observed (Fig. S26†). We speculate, on the basis of the above experimental results, that ESY and RB could be absorbed and encapsulated into the pores of the PAL matrix, significantly shortening the distance between CsPbBr$_3$ QDs and ESY/RB, which guaranteed more efficient energy transfer.

It is well known that ESY and RB dyes, as efficient photosensitizers, can be utilized for green chemical synthesis.[71–74] In this context, to explore the utilization of the ALHS with sequential two-step FRET as a sustainable energy source, the photocatalytic activity of the RB-ESY-CsPbBr$_3$@PAL system is evaluated by catalyzing the Friedel–Crafts alkylation reactions between indol (1a) and N,N-dimethylaniline (b) in an aqueous solution ($V_{water} : V_{MeCN} = 1 : 1$, considering the solubility of the substrates) under visible light (Xe lamp as the sunlight simulator) to synthesize the target product 4-(1H-indol-3-ylmethyl)-N,N-dimethylaniline (1c) that is an important structural skeleton in various naturally occurring products and pharmaceuticals (Fig. S27†).[75,76] The CsPbBr$_3$@PAL composite can act as an efficient antenna to harvest UV/Vis light and pass photoexcitation to ESY and RB successively through the sequential two-step FRET mechanism, where it is utilized to

Table 1 Photocatalytic Friedel–Crafts alkylation in aqueous solution

Entry	Catalyst	Light	Solvent	Isolated yield%
1[a]	ESY + RB	Yes	H$_2$O : CH$_3$CN = 1 : 1	26.7
2	CsPbBr$_3$@PAL	Yes	H$_2$O : CH$_3$CN = 1 : 1	7.4
3[a]	ALHS	Yes	H$_2$O : CH$_3$CN = 1 : 1	65.5
4[a]	ALHS	No	H$_2$O : CH$_3$CN = 1 : 1	Trace
5[b]	RB	Yes	CH$_3$CN : H$_2$O = 4 : 1	52

[a] 1.03×10^{-6} mol% catalyst at room temperature for 12 h (this work). [b] 5 mol% catalyst at room temperature for 24 h.[7]

synthesize value chemicals (Fig. S28†). Hence, the solar energies can be directly transformed. The Friedel–Crafts alkylation reaction was carried out by ^{1}H NMR spectroscopy (Fig. S29†), and the targeted product was isolated and purified by column chromatography on silica gel. As presented in Table 1, when RB-ESY-CsPbBr$_3$@PAL functions as a nanoreactor, the yield of 1c reached 65.5% after 12 h irradiation under optimized conditions. Inversely, only 26.7% and 7.4% yields were collected by using ESY/RB dyes and CsPbBr$_3$@PAL under otherwise identical conditions, respectively. In addition, the amount of organic photocatalyst and photocatalytic reaction time in this catalytic system are much lower than those reported in the literature.[73] Moreover, no photocatalytic activity was exhibited when the reaction was performed in the absence of light. The RB-ESY-CsPbBr$_3$@PAL system as a nanoreactor not only conspicuously enhanced the reaction yield but also successfully fulfilled the Friedel–Crafts alkylation reaction in aqueous solution. In addition, the system did not undergo dye photobleaching in the catalytic reaction process owing to the protection of the PAL matrix (Fig. S27†). Furthermore, to evaluate the scope of the RB-ESY-CsPbBr$_3$@PAL system as a nanoreactor, the reactivities of indoles bearing an electron-donating group (methyl) and bearing an electron-withdrawing group (bromine) and N,N-dimethylaniline to afford 3-arylmethyl indole derivatives were investigated, respectively (shown in Fig. S30 and S31†). The light-harvesting RB-ESY-CsPbBr$_3$@PAL system exhibits higher photocatalytic activities compared to dye alone (Table S7†). The excellent photocatalytic activity of the RB-ESY-CsPbBr$_3$@PAL system in aqueous solution results from three possible factors: (i) the PAL matrix as a protection shell endows CsPbBr$_3$ QDs with ultrastability in water. In addition, in situ encapsulation and defect passivation of the PAL matrix make CsPbBr$_3$@PAL show an enhanced quantum yield and a longer fluorescence lifetime compared to CsPbBr$_3$ QDs in water. (ii) The RB-ESY-CsPbBr$_3$@PAL system with sequential two-step FRET could elevate the utilization efficiency of solar energy. (iii) Loading ESY/RB into the channels of the PAL matrix and assembling into the surface of the perovskite QDs can reduce photobleaching, improve energy transfer, and shorten the distance between the donor and the acceptor. These results suggested that the ESY-RB-CsPbBr$_3$@PAL system could

make full utilization of the captured solar photons to effectively photocatalyze the chemical reaction in aqueous medium, which presents a versatile approach to enhance the photocatalytic activities of photosensitizers.

3. Conclusions

In summary, a water-resistant perovskite–palygorskite light-harvesting antenna has been successfully synthesized by *in situ* passivating and encapsulating CsPbBr$_3$ QDs into the pores of a natural PAL matrix. Experimental data and molecular dynamics simulations showed that the PAL in CsPbBr$_3$@PAL could efficiently prevent the contact between water and CsPbBr$_3$ QDs, which greatly improved the structural stability of CsPbBr$_3$ QDs under an external harsh environment, including exposure to ambient air conditions, heat (150 °C), and upon immersion in water for more than 30 days. Meanwhile, the synergy of *in situ* encapsulation of the PAL matrix and defect passivation caused by H-bonding and coordination-bonding interactions contributes to excellent luminescence for the CsPbBr$_3$ QDs with a QY value of 36.2% in water and a longer exciton lifetime, which is the highest value among the porous matrices emasculated CsPbBr$_3$ QDs. Furthermore, by introducing Cl and I halogen anions, other halide perovskites could successfully load into the PAL matrix, and thus the formed CsPbX$_3$@PAL composites accurately achieve color tunable emission under the excitation of UV light. The above advantages make CsPbX$_3$@PAL a good light-harvesting antenna to sequentially assemble ESY and RB for constructing an efficient light-harvesting system in water. The experimental results showed that RB-ESY-CsPbBr$_3$@PAL exhibited extremely enhanced photocatalytic activity toward Friedel–Crafts alkylation reactions in aqueous solution, 2.5-fold higher than that of corresponding ESY/RB. Our reported interface engineering and encapsulation strategy with natural PAL will provide an alternative route to fabricate stable and efficient perovskite based artificial light-harvesting systems in aqueous media for solar-energy conversion.

4. Experimental

4.1 Preparation of acid-activated palygorskite

Natural palygorskite (PAL) was premodified by acid activation according to the protocol described in the previous literature.[47,77] Typically, 5 g of natural PAL micro-powder was soaked in 50 mL of HCl aqueous solution with a concentration of 5 M and was stirred vigorously at 80 °C for 1 h under reflux. After this, heating was stopped and the sample was maintained for 4 h in acid solution at room temperature. Subsequently, the acid-activated PAL was washed using deionized water until pH ~ 6 and dried at 105 °C overnight. The final sample is denoted as PAL. The purpose of acid modified PAL is to eliminate mineral impurities and increase silanol groups (Si–OH).

4.2 Preparation of PbBr$_2$@PAL

0.5 mmol of PbBr$_2$ was dissolved in 10 mL of DMF. DMF acted as a good solvent to dissolve inorganic salts. Then, 100 mg of porous resultant PAL matrix materials was soaked in 1.0 mL of the precursor solution at 80 °C for 7 days. Subsequently, DMF/ethanol was utilized to centrifugally wash away free PbBr$_2$ attached to the surface of the PAL matrix. About 110 mg of solid powder was obtained by vacuum drying. The synthesis of PbX$_2$@PAL (X = Cl, I) was similar to that of PbBr$_2$@PAL.

4.3 Preparation of the CsPbBr$_3$@PAL antenna

The as-prepared PbBr$_2$@PAL (110 mg) was immersed in 200 μL of Cs-Oleate DMF solution (50 mM) under ultrasound, and then stirred vigorously for 1 h. After that, the CsPbBr$_3$@PAL composite was prepared by putting the above reaction mixture into 10.0 mL dried PhMe. Finally, the CsPbBr$_3$@PAL antenna was obtained after washing with PhMe. About 118 mg of solid powder was obtained by vacuum drying. The synthesis of CsPbX$_3$@PAL (X = Cl, I) was similar to that of CsPbX$_3$@PAL.

4.4 Preparation of the ESY-CsPbBr$_3$@PAL assembly

The as-prepared PbBr$_2$@PAL (110 mg) was immersed in 300 μL of DMF solution containing dye ESY (8.2 mg) under vigorous stirring for 1 h. Subsequently, 200 μL of Cs-Oleate DMF solution (50 mM) was added to the above mixture to obtain the ESY-CsPbX$_3$@PAL precursor. Then, the reaction mixture was soaked in 10.0 mL dried PhMe to prepare the ESY-CsPbBr$_3$@PAL assembly.

4.5 Preparation of the RB-ESY-CsPbBr$_3$@PAL system

The as-prepared PbBr$_2$@PAL (110 mg) was immersed in 300 μL of DMF solution containing ESY (8.2 mg) and RB (10.6 mg) under vigorous stirring for 1 h. Subsequently, 200 μL of Cs-Oleate DMF solution (50 mM) was added to the above mixture to obtain the RB-ESY-CsPbX$_3$@PAL precursor. Then, the reaction mixture was soaked in 10.0 mL dried PhMe to prepare the RB-ESY-CsPbBr$_3$@PAL system.

Data availability

All the data supporting this article have been included in the main text and the ESI.†

Author contributions

B. D. W. designed and conceived the whole project. A. Q. W and S. Y. L. conceived the project. G. P. M. carried out the materials synthesis, experimental test and data analysis. M. X. J. conducted molecular dynamics simulations. L. P. Z., G. P. M., J. H. and B. D. W. wrote the paper together. Z. F. Z. and T. Z. H. performed the electron microscopy tests. All the authors contributed to the discussion during the whole project.

Conflicts of interest

There are no conflicts to declare.

Acknowledgements

Notes and references

1 C. D. P. Duffy, *Science*, 2020, **368**, 1427–1428.
2 R. Croce and H. van Amerongen, *Nat. Chem. Biol.*, 2014, **10**, 492–501.
3 N. Nelson and A. Ben-Shem, *Nat. Rev. Mol. Cell Biol.*, 2004, **5**, 971–982.
4 Y. Kuramochi, R. Sato, H. Sakuma and A. Satake, *Chem. Sci.*, 2022, **13**, 9861–9879.
5 Y. Ishida, T. Shimada, D. Masui, H. Tachibana, H. Inoue and S. Takagi, *J. Am. Chem. Soc.*, 2011, **133**, 14280–14286.
6 X. Qian, Y. Zhao, Y. Alsaid, X. Wang, M. Hua, T. Galy, H. Gopalakrishna, Y. Yang, J. Cui, N. Liu, M. Marszewski, L. Pilon, H. Jiang and X. He, *Nat. Nanotechnol.*, 2019, **14**, 1048–1055.
7 X.-B. Li, C.-H. Tung and L.-Z. Wu, *Nat. Rev. Chem.*, 2018, **2**, 160–173.
8 D. Zhang, W. Yu, S. Li, Y. Xia, X. Li, Y. Li and T. Yi, *J. Am. Chem. Soc.*, 2021, **143**, 1313–1317.
9 H.-J. Yu, X.-L. Zhou, X. Dai, F.-F. Shen, Q. Zhou, Y.-M. Zhang, X. Xu and Y. Liu, *Chem. Sci.*, 2022, **13**, 8187–8192.
10 A. H. Proppe, Y. C. Li, A. Aspuru-Guzik, C. P. Berlinguette, C. J. Chang, R. Cogdell, A. G. Doyle, J. Flick, N. M. Gabor, R. van Grondelle, S. Hammes-Schiffer, S. A. Jaffer, S. O. Kelley, M. Leclerc, K. Leo, T. E. Mallouk, P. Narang, G. S. Schlau-Cohen, G. D. Scholes, A. Vojvodic, V. W.-W. Yam, J. Y. Yang and E. H. Sargent, *Nat. Rev. Mater.*, 2020, **5**, 828–846.
11 Z. Fan, Y. Yin, B. Cai, Q. Ma, Q. Liu, X. Liu, L. Yinhua and W.-H. Zhang, *Chem. Sci.*, 2022, **13**, 10512–10522.
12 A. Starkholm, L. Kloo and P. H. Svensson, *J. Am. Chem. Soc.*, 2020, **142**, 18437–18448.
13 X. Zhang, Y. Xu, F. Giordano, M. Schreier, N. Pellet, Y. Hu, C. Yi, N. Robertson, J. Hua, S. M. Zakeeruddin, H. Tian and M. Gratzel, *J. Am. Chem. Soc.*, 2016, **138**, 10742–10745.
14 L. Hu, Q. Zhao, S. Huang, J. Zheng, X. Guan, R. Patterson, J. Kim, L. Shi, C. H. Lin, Q. Lei, D. Chu, W. Tao, S. Cheong, R. D. Tilley, A. W. Y. Ho-Baillie, J. M. Luther, J. Yuan and T. Wu, *Nat. Commun.*, 2021, **12**, 466.
15 N. Melnychuk, S. Egloff, A. Runser, A. Reisch and A. S. Klymchenko, *Angew. Chem., Int. Ed.*, 2020, **59**, 6811–6818.
16 Z. Zhang, Z. Zhao, L. Wu, S. Lu, S. Ling, G. Li, L. Xu, L. Ma, Y. Hou, X. Wang, X. Li, G. He, K. Wang, B. Zou and M. Zhang, *J. Am. Chem. Soc.*, 2020, **142**, 2592–2600.
17 X. Zhang, S. Rehm, M. M. Safont-Sempere and F. Wurthner, *Nat. Chem.*, 2009, **1**, 623–629.
18 K. Trofymchuk, A. Reisch, P. Didier, F. Fras, P. Gilliot, Y. Mely and A. S. Klymchenko, *Nat. Photonics*, 2017, **11**, 657–663.
19 Q. Zhang, M. He, Q. Wan, W. Zheng, M. Liu, C. Zhang, X. Liao, W. Zhan, L. Kong, X. Guo and L. Li, *Chem. Sci.*, 2022, **13**, 3719–3727.
20 Y. X. Yuan, J. H. Jia, Y. P. Song, F. Y. Ye, Y. S. Zheng and S. Q. Zang, *J. Am. Chem. Soc.*, 2022, **144**, 5389–5399.
21 X. M. Chen, Q. Cao, H. K. Bisoyi, M. Wang, H. Yang and Q. Li, *Angew. Chem., Int. Ed.*, 2020, **59**, 10493–10497.
22 Y. X. Hu, X. Hao, L. Xu, X. Xie, B. Xiong, Z. Hu, H. Sun, G. Q. Yin, X. Li, H. Peng and H. B. Yang, *J. Am. Chem. Soc.*, 2020, **142**, 6285–6294.
23 Q. Song, S. Goia, J. Yang, S. C. L. Hall, M. Staniforth, V. G. Stavros and S. Perrier, *J. Am. Chem. Soc.*, 2021, **143**, 382–389.
24 Y. Shen, L. P. Cheng, Y. Q. Li, W. Li, J. D. Chen, S. T. Lee and J. X. Tang, *Adv. Mater.*, 2019, **31**, e1901517.
25 J. Yuan, X. Zhang, J. Sun, R. Patterson, H. Yao, D. Xue, Y. Wang, K. Ji, L. Hu, S. Huang, D. Chu, T. Wu, J. Hou and J. Yuan, *Adv. Funct. Mater.*, 2021, **31**(27), 2101272.
26 K. L. Wang, Y. H. Zhou, Y. H. Lou and Z. K. Wang, *Chem. Sci.*, 2021, **12**, 11936–11954.
27 K. Chen, W. Jin, Y. Zhang, T. Yang, P. Reiss, Q. Zhong, U. Bach, Q. Li, Y. Wang, H. Zhang, Q. Bao and Y. Liu, *J. Am. Chem. Soc.*, 2020, **142**, 3775–3783.
28 A. Dey, J. Ye, A. De, E. Debroye, S. K. Ha, E. Bladt, A. S. Kshirsagar, Z. Wang, J. Yin, Y. Wang, L. N. Quan, F. Yan, M. Gao, X. Li, J. Shamsi, T. Debnath, M. Cao, M. A. Scheel, S. Kumar, J. A. Steele, M. Gerhard, L. Chouhan, K. Xu, X.-g. Wu, Y. Li, Y. Zhang, A. Dutta, C. Han, I. Vincon, A. L. Rogach, A. Nag, A. Samanta, B. A. Korgel, C.-J. Shih, D. R. Gamelin, D. H. Son, H. Zeng, H. Zhong, H. Sun, H. V. Demir, I. G. Scheblykin, I. Mora-Seró, J. K. Stolarczyk, J. Z. Zhang, J. Feldmann, J. Hofkens, J. M. Luther, J. Pérez-Prieto, L. Li, L. Manna, M. I. Bodnarchuk, M. V. Kovalenko, M. B. J. Roeffaers, N. Pradhan, O. F. Mohammed, O. M. Bakr, P. Yang, P. Müller-Buschbaum, P. V. Kamat, Q. Bao, Q. Zhang, R. Krahne, R. E. Galian, S. D. Stranks, S. Bals, V. Biju, W. A. Tisdale, Y. Yan, R. L. Z. Hoye and L. Polavarapu, *ACS Nano*, 2021, **15**, 10775–10981.
29 J. De Roo, M. Ibanez, P. Geiregat, G. Nedelcu, W. Walravens, J. Maes, J. C. Martins, I. Van Driessche, M. V. Kovalenko and Z. Hens, *ACS Nano*, 2016, **10**, 2071–2081.
30 Q. A. Akkerman, G. Raino, M. V. Kovalenko and L. Manna, *Nat. Mater.*, 2018, **17**, 394–405.
31 X. Han, Y. Lei, Q. Liao and H. Fu, *Angew. Chem., Int. Ed.*, 2021, **60**, 3037–3046.
32 H. Zhang, Y. Wu, Q. Liao, Z. Zhang, Y. Liu, Q. Gao, P. Liu, M. Li, J. Yao and H. Fu, *Angew. Chem., Int. Ed.*, 2018, **57**, 7748–7752.
33 G. Meng, L. Zhen, S. Sun, J. Hai, Z. Zhang, D. Sun, Q. Liu and B. Wang, *J. Mater. Chem. A*, 2021, **9**, 24365–24373.

34 K. Zhong, S. Lu, W. Guo, J. Su, S. Sun, J. Hai, F. Chen, A. Wang and B. Wang, *J. Mater. Chem. A*, 2021, **9**, 10180–10185.

35 M. V. Kovalenko, L. Protesescu and M. I. Bodnarchuk, *Science*, 2017, **358**, 745–750.

36 Q. Zhang and Y. Yin, *ACS Cent. Sci.*, 2018, **4**, 668–679.

37 Y. Wei, X. Deng, Z. Xie, X. Cai, S. Liang, P. a. Ma, Z. Hou, Z. Cheng and J. Lin, *Adv. Funct. Mater.*, 2017, **27**, 1703535.

38 A. Loiudice, S. Saris, E. Oveisi, D. T. L. Alexander and R. Buonsanti, *Angew. Chem., Int. Ed.*, 2017, **56**, 10696–10701.

39 P. Wang, B. Wang, Y. Liu, L. Li, H. Zhao, Y. Chen, J. Li, S. F. Liu and K. Zhao, *Angew. Chem., Int. Ed.*, 2020, **59**, 23100–23106.

40 J. Hou, P. Chen, A. Shukla, A. Krajnc, T. Wang, X. Li, R. Doasa, L. H. G. Tizei, B. Chan, D. N. Johnstone, R. Lin, T. U. Schülli, I. Martens, D. Appadoo, M. S. Ari, Z. Wang, T. Wei, S.-C. Lo, M. Lu, S. Li, E. B. Namdas, G. Mali, A. K. Cheetham, S. M. Collins, V. Chen, L. Wang and T. D. Bennett, *Science*, 2021, **374**, 621–625.

41 W. F. Bradley, *Am. Mineral.*, 1940, **25**, 405–410.

42 W. L. Haden and A. Schwint, *Ind. Eng. Chem.*, 1967, **59**, 58–69.

43 W. T. Granquist and R. C. Amero, *J. Am. Chem. Soc.*, 1948, **70**, 3265–3270.

44 B. Mu, Y. Kang and A. Wang, *J. Mater. Chem. A*, 2013, **1**, 4804–4811.

45 H. Guo, H. Zhang, F. Peng, H. Yang, L. Xiong, C. Huang, C. Wang, X. Chen and L. Ma, *Appl. Clay Sci.*, 2015, **111**, 83–89.

46 X.-Y. Li, D.-Y. Zhang, X.-Q. Liu, L.-Y. Shi and L.-B. Sun, *Chem. Eng. Sci.*, 2016, **141**, 184–194.

47 W. Wang, W. Dong, G. Tian, L. Sun, Q. Wang, A. Hui, B. Mu and A. Wang, *Powder Technol.*, 2019, **354**, 1–10.

48 M. K. Uddin, *Chem. Eng. J.*, 2017, **308**, 438–462.

49 L. Wang, Y. Shi, D. Yao, H. Pan, H. Hou, J. Chen and J. C. Crittenden, *Chem. Eng. J.*, 2019, **366**, 569–576.

50 A. Kilincarslan Kaygun, M. Eral and S. Akyil Erenturk, *J. Radioanal. Nucl. Chem.*, 2016, **311**, 1459–1464.

51 X. Liu, X. Xu, J. Sun, A. Alsaedi, T. Hayat, J. Li and X. Wang, *Chem. Eng. J.*, 2018, **343**, 217–224.

52 H. Chen, J. Zhao, A. Zhong and Y. Jin, *Chem. Eng. J.*, 2011, **174**, 143–150.

53 T. Chen, H. Liu, J. Li, D. Chen, D. Chang, D. Kong and R. L. Frost, *Chem. Eng. J.*, 2011, **166**, 1017–1021.

54 W. Kuang, G. A. Facey and C. Detellier, *Clays Clay Miner.*, 2004, **52**, 635–642.

55 Y. C. Zou, L. Mogg, N. Clark, C. Bacaksiz, S. Milovanovic, V. Sreepal, G. P. Hao, Y. C. Wang, D. G. Hopkinson, R. Gorbachev, S. Shaw, K. S. Novoselov, R. Raveendran-Nair, F. M. Peeters, M. Lozada-Hidalgo and S. J. Haigh, *Nat. Mater.*, 2021, **20**, 1677–1682.

56 L. Mogg, G. P. Hao, S. Zhang, C. Bacaksiz, Y. C. Zou, S. J. Haigh, F. M. Peeters, A. K. Geim and M. Lozada-Hidalgo, *Nat. Nanotechnol.*, 2019, **14**, 962–966.

57 S. Sun, D. Yuan, Y. Xu, A. Wang and Z. Deng, *ACS Nano*, 2016, **10**, 3648–3657.

58 G. Y. Qiao, D. Guan, S. Yuan, H. Rao, X. Chen, J. A. Wang, J. S. Qin, J. J. Xu and J. Yu, *J. Am. Chem. Soc.*, 2021, **143**, 14253–14260.

59 X. Li, M. I. Dar, C. Yi, J. Luo, M. Tschumi, S. M. Zakeeruddin, M. K. Nazeeruddin, H. Han and M. Gratzel, *Nat. Chem.*, 2015, **7**, 703–711.

60 J. Yang, E. H. Sargent, S. O. Kelley and J. Y. Ying, *Nat. Mater.*, 2009, **8**, 683–689.

61 X. Yu, L. Wu, D. Yang, M. Cao, X. Fan, H. Lin, Q. Zhong, Y. Xu and Q. Zhang, *Angew. Chem., Int. Ed.*, 2020, **59**, 14527–14532.

62 Y. Liu, Z. Yang, D. Cui, X. Ren, J. Sun, X. Liu, J. Zhang, Q. Wei, H. Fan, F. Yu, X. Zhang, C. Zhao and S. F. Liu, *Adv. Mater.*, 2015, **27**, 5176–5183.

63 L. Xie, Z. Hong, J. Zan, Q. Wu, Z. Yang, X. Chen, X. Ou, X. Song, Y. He, J. Li, Q. Chen and H. Yang, *Adv. Mater.*, 2021, **33**, e2101852.

64 V. Malgras, S. Tominaka, J. W. Ryan, J. Henzie, T. Takei, K. Ohara and Y. Yamauchi, *J. Am. Chem. Soc.*, 2016, **138**, 13874–13881.

65 K. Tanaka, T. Takahashi, T. Ban, T. Kondo, K. Uchida and N. Miura, *Solid State Commun.*, 2003, **127**, 619–623.

66 X. Peng, J. Wickham and A. P. Alivisatos, *J. Am. Chem. Soc.*, 1998, **120**, 5343–5344.

67 Y. Yin and A. P. Alivisatos, *Nature*, 2005, **437**, 664–670.

68 V. Adinolfi, O. Ouellette, M. I. Saidaminov, G. Walters, A. L. Abdelhady, O. M. Bakr and E. H. Sargent, *Adv. Mater.*, 2016, **28**, 7264–7268.

69 T. Niu, J. Lu, R. Munir, J. Li, D. Barrit, X. Zhang, H. Hu, Z. Yang, A. Amassian, K. Zhao and S. F. Liu, *Adv. Mater.*, 2018, **30**, e1706576.

70 S. Wu, Z. Li, M. Q. Li, Y. Diao, F. Lin, T. Liu, J. Zhang, P. Tieu, W. Gao, F. Qi, X. Pan, Z. Xu, Z. Zhu and A. K. Jen, *Nat. Nanotechnol.*, 2020, **15**, 934–940.

71 X. Z. Fan, J. W. Rong, H. L. Wu, Q. Zhou, H. P. Deng, J. D. Tan, C. W. Xue, L. Z. Wu, H. R. Tao and J. Wu, *Angew. Chem., Int. Ed.*, 2018, **57**, 8514–8518.

72 D. M. Yan, J. R. Chen and W. J. Xiao, *Angew. Chem., Int. Ed.*, 2019, **58**, 378–380.

73 A. Srivastava, P. K. Singh, A. Ali, P. P. Singh and V. Srivastava, *RSC Adv.*, 2020, **10**, 39495–39508.

74 X.-Q. Dai, W.-X. Xu, Y.-L. Wen, X.-H. Liu and J.-Q. Weng, *Tetrahedron Lett.*, 2018, **59**, 2945–2949.

75 R. Contractor, I. J. Samudio, Z. Estrov, D. Harris, J. A. McCubrey, S. H. Safe, M. Andreeff and M. Konoplev, *Cancer Res.*, 2005, **65**, 2890–2898.

76 M. Lounasmaa and A. Tolvanen, *Nat. Prod. Rep.*, 2000, **17**, 175–191.

77 H. Chen, Y. Zhaoa and A. Wang, *J. Hazard. Mater.*, 2007, **149**, 346–354.